Journal of the Optical Society of America B
OPTICAL PHYSICS

Gain dynamics in a highly ytterbium-doped potassium double tungstate epitaxial layer

Yean-Sheng Yong,[1,*] Shanmugam Aravazhi,[2] Sergio A. Vázquez-Córdova,[1] Jennifer L. Herek,[1] Sonia M. García-Blanco,[1] and Markus Pollnau[2,3]

[1]Optical Sciences Group, MESA+ Institute for Nanotechnology, University of Twente, P.O. Box 217, 7500 AE Enschede, The Netherlands
[2]Integrated Optical Microsystems Group, MESA+ Institute for Nanotechnology, University of Twente, P.O. Box 217, 7500 AE Enschede, The Netherlands
[3]Advanced Technology Institute, Department of Electrical and Electronic Engineering, University of Surrey, Guildford GU2 7XH, UK
*Corresponding author: y.s.yong@utwente.nl

Received 31 May 2018; revised 23 July 2018; accepted 23 July 2018; posted 24 July 2018 (Doc. ID 333041); published 21 August 2018

Active media with high rare-earth concentrations are essential for small-footprint waveguide amplifiers. When operating at high population inversion, such devices are often affected by undesired energy-transfer processes and thermal effects. In this work, we study a 32-μm-thick epitaxial layer of $KGd_{0.43}Yb_{0.57}(WO_4)_2$, representing an Yb^{3+} concentration of $\sim 3.8 \times 10^{21}$ cm^{-3}, grown on an undoped $KY(WO_4)_2$ substrate. The pump absorption, luminescence decay, and small-signal gain are investigated under intense pumping conditions. Spectroscopic signatures of an energy-transfer process and of quenched ions, as well as thermal effects, are observed. We present a gain model which takes into account excessive heat generated due to the abovementioned experimental observations. Based on finite-element calculations, we find that the net gain is significantly reduced due to, first, a fraction of Yb^{3+} ions not contributing to stimulated emission, second, a reduction of population inversion owing to a parasitic energy-transfer process and, third, degradation of the effective transition cross-sections owing to device heating. Nevertheless, a signal enhancement of 8.1 dB was measured from the sample at 981 nm wavelength when pumping at 932 nm. The corresponding signal net gain of ~800 dB/cm, which was achieved without thermal management, is promising for a waveguide amplifier operating without active cooling.

OCIS codes: (160.5690) Rare-earth-doped materials; (130.3130) Integrated optics materials; (140.4480) Optical amplifiers; (140.3615) Lasers, ytterbium.

https://doi.org/10.1364/JOSAB.35.002176

1. INTRODUCTION

Potassium rare-earth double tungstate crystals doped with trivalent ytterbium, $KRE(WO_4)_2:Yb^{3+}$, have been widely used for microchip [1,2], mode-locked [3], and high-power lasers [4,5]. The $KRE(WO_4)_2:Yb^{3+}$ gain medium exhibits transition cross-sections significantly higher than those of many other Yb^{3+}-doped materials, such as YAG:Yb^{3+} [6,7]. By use of a lattice-engineering approach [8–10], a crystalline waveguiding epitaxial layer with high amounts of Yb^{3+} ions can be grown onto an undoped $KY(WO_4)_2$ substrate, enabling efficient continuous-wave (CW) [11] and *Q*-switched [12–14] $KRE(WO_4)_2:Yb^{3+}$ planar waveguide lasers. By further micro-structuring of the $KRE(WO_4)_2:Yb^{3+}$ waveguide layer, low-threshold [15], high-efficiency [16], and tunable [17] channel waveguide lasers can be realized. With such an approach, a record-high net gain of 935 dB/cm at 981 nm wavelength was achieved in a $KRE(WO_4)_2$ waveguide amplifier with 47.5 at. % Yb^{3+}, which is equivalent to a concentration as high as $\sim 3.0 \times 10^{21}$ cm^{-3} [18]. Such a compact waveguide amplifier operating at ~1000 nm wavelength is beneficial for scaling of short-reach interconnects in photonic integrated circuits, high-performance computing systems, and data centers [19–22]. As the net gain achieved in $KRE(WO_4)_2:Yb^{3+}$ is more than an order-of-magnitude higher than those of other singly doped Nd^{3+} or Yb^{3+} gain media [23–26], it is worthwhile to investigate the gain properties of $KRE(WO_4)_2:Yb^{3+}$ epitaxial layers with further increased Yb^{3+} concentration.

Operating a heavily doped device under high excitation density is known to be challenging and often inhibited by various undesired effects. For instance, a power-dependent nonexponential decay behavior was reported in YbAG crystals, indicating the presence of a parasitic energy-transfer process [27]. Besides, quenched ions with a short excited-state lifetime were identified in various Er^{3+}- [28–31] and Yb^{3+}-doped [32–34] materials. These ions are normally not detected in lifetime

measurements and do not reveal their quenched nature in small-signal absorption measurements but can induce nonsaturable pump absorption [28,34]. In addition, various abnormalities associated with thermal effects were reported in thin-disc gain media with high Yb^{3+} concentrations. For example, an additional decay process with large heat generation was observed in a YAG:Yb^{3+} laser at high excitation density, resulting in limited gain and reduced laser efficiency [35]. Besides, excessive heat generation leading to the termination of CW operation and a rapid decline in lasing power [36] was observed in a laser based on a $KLu(WO_4)_2$:(52 at. %)Yb^{3+} epitaxial layer. A similar observation was reported from laser experiments in a $KYb(WO_4)_2$ crystal, in which a short pump-pulse duration was needed to minimize thermal effects [37]. Thus far, most of these abnormalities were studied based on device performance. There are limited reports on the investigation of their origin [38] and their correlation with device performance.

In this work, we investigate the gain dynamics in a $KGd_{0.43}Yb_{0.57}(WO_4)_2$ (i.e., 57 at. % Yb^{3+}) epitaxial layer, representing a high ytterbium concentration of $\sim 3.8 \times 10^{21}$ cm^{-3}. Power-dependent luminescence-decay and pump-absorption measurements are performed to identify potential energy-transfer and fast quenching processes. In addition, a gain model which accounts for an energy-transfer process, quenched ions, and thermal effects is established. The modeled and experimental gain results are compared to obtain further insight into the achievable gain in $KGd_{0.43}Yb_{0.57}(WO_4)_2$ without thermal management.

2. EXPERIMENTAL

A $KGd_{0.43}Yb_{0.57}(WO_4)_2$ layer was grown onto a commercially available *b*-oriented, 1 mm × 10 mm × 10 mm $KY(WO_4)_2$ substrate (Altechna) by liquid-phase epitaxy [6,10]. The rear surface of the sample was lapped and polished to remove the excess growth layer, whereas its front surface was lapped and polished parallel to the substrate, resulting in a final layer thickness of ~32 μm [6]. The prepared active layer is considerably thicker than layers typically used for waveguide devices (~2–6 μm) in order to allow direct examination of the material characteristics by launching optical beams perpendicular to the layer. The sample was mounted on a small holder made of thin copper plates with a clear aperture of ~8.6 mm × 8.6 mm. No special thermal management was applied to the sample during all measurements.

A confocal luminescence lifetime measurement setup [39] was used for power-dependent luminescence-decay measurements. The nondestructive confocal measurement suppresses radiation trapping [40] via a small pumped volume and discrimination of re-emitted luminescence from the unpumped region. In addition, it allows for investigation of the decay-time behavior under high excitation density, which is similar to the operating condition of an amplifier. A diode laser wavelength-stabilized by a fiber Bragg grating at 981 nm wavelength (Gooch & Housego) was used as the excitation source. The excitation beam was modulated at 233 Hz with 50% duty cycle using a laser diode controller (Newport 6100) to allow for complete relaxation of the Yb^{3+} ions between two excitation pulses. The laser diode was used for lifetime measurements, because its electronically modulated output beam possesses a consistent, short fall time throughout the experiment.

The experimental setup used for signal-enhancement measurement is shown in Fig. 1. A CW Ti:Sapphire laser (Spectra-Physics 3900S) tuned to 932 nm wavelength was used as the pump source. By pumping at the local absorption peak of $KGd_{0.43}Yb_{0.57}(WO_4)_2$ at ~932 nm, the high emission cross-section at ~981 nm [6] can be leveraged for signal amplification. The pump power was controlled by a half-wave plate and a Glan polarizer. The signal beam at ~981 nm wavelength with a bandwidth ≤ 1 nm was obtained with a supercontinuum light source (Fianium SC-450) passing through a monochromator. It was mechanically chopped at 233 Hz for lock-in detection to discriminate the detected 981 nm wavelength signal from spontaneous emission produced by the sample and from different background noise sources. A small launched signal power (<100 nW) was used to ensure signal amplification within the small-signal-gain regime. Both pump and signal beams were combined using a dichroic mirror and subsequently focused perpendicularly onto the sample at $E \| N_m$ polarization using a microscope objective (MO). To ensure a good overlap of pump and signal beams, the foci were characterized using a beam profiler (Thorlabs BP209) mounted onto a motorized linear stage, and the beam-expander optics were adjusted for optimal beam overlap prior to the experiment. The residual optical beams passing through the sample were collected using another MO and subsequently directed to a light guide which was connected to a spectrometer (Jobin Yvon iHR550) equipped with a cooled InGaAs detector. The combination of a high-performance pump filter (Techspec #66-238) with cutoff wavelength at 950 nm and a dispersive grating in the spectrometer ensured that the residual pump power was much lower than the 981 nm wavelength signal power. The lock-in signals recorded with and without pumping were used to evaluate the signal enhancement.

Pump-transmission measurements were performed using the setup shown in Fig. 1, with only the pump beam switched on, to deduce the pump power absorbed by the sample. The pump power at 932 nm wavelength was measured using a thermopile (Coherent FieldMaxII, PM10) before the incident MO and after the collection MO. The launched and absorbed pump powers were deduced after correcting for the objective transmittances and Fresnel reflections on the sample.

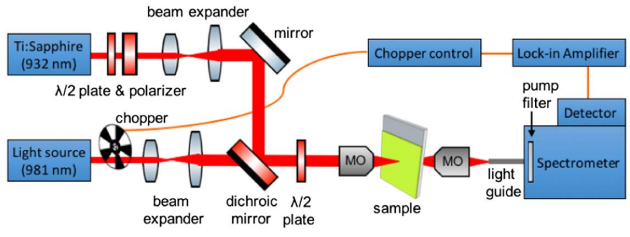

Fig. 1. Schematic of pump–probe measurement setup. The signal-enhancement measurement was performed using a 932 nm pump beam and 981 nm signal beam. The same setup was used to measure pump absorption and luminescence spectra with only the pump beam. The abbreviation MO represents the microscope objective.

The forward-propagating near-infrared luminescence spectra were measured using the same setup as shown in Fig. 1 in a separate experiment by launching only the pump beam into the sample. The recorded luminescence spectra were corrected for spectral response of the detection system determined using a calibration lamp (Ocean Optics LS-1-CAL).

3. GAIN MODEL

Since the energy-level scheme of the Yb^{3+} ion consists only of the $^2F_{7/2}$ ground-state and the $^2F_{5/2}$ excited-state manifolds, a two-level system is used to model the gain and loss of optical beams. This is based on the consideration that the Yb^{3+} ions excited to the upper Stark level of the $^2F_{5/2}$ manifold undergo rapid relaxation to the lower Stark level of the same manifold within a time scale much shorter than the excited-state lifetime. Hence, the quasi-three-level system can be modeled with only two energy levels.

The gain model presented in this work is modified from [28]. It takes into account two distinct classes of Yb^{3+} ions, namely, active ions and quenched ions, which participate in pump absorption. The active ions decay by infrared luminescence to the ground state with an excited-state luminescence lifetime τ_a. The quenched ions, on the other hand, have a nonradiative lifetime τ_q which is significantly shorter than τ_a. The total density of active and quenched ions residing in the ground state and excited state follows

$$N_{0a/q} + N_{1a/q} = f_{a/q} N_{\mathrm{Yb}}, \tag{1}$$

where N_{Yb} is the density of Yb^{3+} ions and N_0 and N_1 are the respective density of ions in the ground state and excited state. The subscripts a and q indicate active and quenched ions, respectively. $f_{a/q}$ represents the fraction of active or quenched ions, with the boundary condition of $f_a + f_q = 1$.

The rate constants of absorption and stimulated emission on the 932 nm pump transition, $R_{p,01}$ and $R_{p,10}$, and the 981 nm signal transition, $R_{s,01}$ and $R_{s,10}$, respectively, are calculated as [41,42]

$$R_{p,01} = I_p \sigma_{\mathrm{abs}}(\lambda_p, T) \cdot \frac{\lambda_p}{hc}, \tag{2a}$$

$$R_{p,10} = I_p \sigma_{\mathrm{em}}(\lambda_p, T) \cdot \frac{\lambda_p}{hc}, \tag{2b}$$

$$R_{s,01} = I_s \sigma_{\mathrm{abs}}(\lambda_s, T) \cdot \frac{\lambda_s}{hc}, \tag{2c}$$

$$R_{s,10} = I_s \sigma_{\mathrm{em}}(\lambda_s, T) \cdot \frac{\lambda_s}{hc}, \tag{2d}$$

where I represents the optical intensity in $\mathrm{W/m^2}$, h is Planck's constant, and c is the speed of light. σ_{abs} and σ_{em} are the effective absorption and emission cross-sections, respectively, at wavelength λ and temperature T. The subscripts p and s denote pump and signal, respectively. Considering that both pump and signal beams possess a Gaussian beam profile in the x–y plane, their lateral intensity profiles, $I_{p,s}$, can be modeled with

$$I_{p,s} = (2P_{p,s}/\pi w_{p,s}^2) \exp[-2(x^2 + y^2)/w_{p,s}^2], \tag{3}$$

where P represents the optical power, and w denotes the Gaussian beam waist. The parameters N, σ, R, and I in Eqs. (1)–(3) are spatially dependent. Although the light path through the active layer is only 32 μm long, the high dopant concentration and large absorption cross-section result in a large fraction of pump light being absorbed, thereby inducing a significant variation of these parameters along the z direction. The xyz discretization for these parameters is taken into account implicitly, but their spatially dependent notation will be omitted in the subsequent discussion.

The rate equations which govern the change of density of the Yb^{3+} ions in the two energy levels are

$$\frac{dN_{1a/q}}{dt} = (R_{p,01} + R_{s,01})N_{0a/q} - (R_{p,10} + R_{s,10})N_{1a/q} - \frac{N_{1a/q}}{\tau_{a/q}} - 2W_{\mathrm{ET}}(N_{1a/q})^2, \tag{4}$$

$$\frac{dN_{0a/q}}{dt} = -\frac{dN_{1a/q}}{dt}. \tag{5}$$

Besides the pump and signal transitions which are typical for the rate equations of Yb^{3+}-doped materials, the model includes an energy-transfer (ET) process identified in our pump-dependent luminescence-decay measurements, which will be shown in Section 4.A. The physical origin of this ET process is currently unknown. However, since the luminescence-decay curves exhibit the typical shape of a Bernoulli curve, see Eq. (7), we chose Grant's model [43], which assumes an infinitely fast energy-migration rate, leading to a "sea" of excitations in the metastable excited state, which are smeared out over the excitation volume. The nonlinear behavior of the ET process is then considered in the rate equations by the term $2W_{\mathrm{ET}}N_1^2$, where W_{ET} is the macroscopic ET parameter in units of $\mathrm{cm^3/s}$, and the factor of 2 accounts for the interaction in which two ions are assumed to leave the excited state. This is similar to a cooperative upconversion process between two neighboring Yb^{3+} ions (although we have not found a clear signature of this process in the visible luminescence spectrum) or an energy-transfer-upconversion process between neighboring Er^{3+} ions in the upper amplifier level [28] (although such a process is not possible in Yb^{3+}). Consequently, the evolution of excited-state population density after cutoff of pump power during luminescence-decay measurements is modeled with [44]

$$\frac{dN_{1a}(t)}{dt} = -\frac{N_{1a}(t)}{\tau_a} - 2W_{\mathrm{ET}}N_{1a}^2(t), \tag{6}$$

which can be solved as

$$N_{1a}(t) = \frac{N_{1a}(0)\exp(-t/\tau_a)}{1 + 2W_{\mathrm{ET}}N_{1a}(0)\tau_a[1 - \exp(-t/\tau_a)]}. \tag{7}$$

$N_{1a}(0)$ represents the density of active excited ions upon cutoff of pump power at time zero. It can be estimated by varying the excitation conditions. The value of W_{ET} can be quantified via simultaneous fitting of luminescence-decay curves measured under different excitation conditions.

The solutions of Eqs. (4) and (5) can be simplified in the case of small-signal amplification. Under such condition, the amplified signal is much weaker than the pump, $I_s \ll I_p$, and does not induce appreciable depletion of population from the excited state. Besides, assuming that τ_q is infinitesimally small, any excited quenched ions will return to the ground state

instantaneously, i.e., $N_{1q} = 0$. In other words, the quenched ions only participate in the absorption of pump and signal photons. These considerations have two direct implications. First, pump absorption and thermal calculations can be de-coupled from the signal loss/gain calculation, because N_1 and N_0 are now dependent only on the pump intensity. As a result, the heat generated in the layer can be calculated by solving the pump absorption and heat generation iteratively. Second, the assumption made on τ_q eases the calculations involving the ET process because the simplified model contains only one quadratic equation.

Under CW pumping, the steady-state condition $dN/dt = 0$ applies. Thus, N_{1a} in Eq. (4) can be solved as

$$N_{1a} = \frac{-B_a + \sqrt{B_a^2 - 4AC_a}}{2A}, \tag{8}$$

where

$$A = 2W_{\mathrm{ET}}, \tag{9a}$$

$$B_a = R_{p,10} + R_{p,01} + \frac{1}{\tau_a}, \tag{9b}$$

$$C_a = -f_a N_{\mathrm{Yb}} R_{p,01}, \tag{9c}$$

for numerical calculations including the ET process, and

$$N_{1a} = \frac{R_{p,01}}{R_{p,01} + R_{p,10} + \tau_a^{-1}}, \tag{10}$$

for numerical calculations excluding the ET process.

The evolution of pump power P_p and signal power P_s along the propagation direction z is calculated according to

$$\frac{dP_p}{dz} = [\sigma_{\mathrm{em},p} N_{1a} - \sigma_{\mathrm{abs},p}(N_{0a} + f_q N_{\mathrm{Yb}})]P_p - \alpha_p P_p, \tag{11}$$

$$\frac{dP_s}{dz} = [\sigma_{\mathrm{em},s} N_{1a} - \sigma_{\mathrm{abs},s}(N_{0a} + f_q N_{\mathrm{Yb}})]P_s - \alpha_s P_s, \tag{12}$$

where $\alpha_{p/s}$ is the propagation-loss coefficient in the medium, and $\sigma_{\mathrm{abs/em},p/s}$ denotes $\sigma_{\mathrm{abs/em}}(\lambda_{p/s}, T)$. Since the propagation loss for devices made of $\mathrm{KRE(WO_4)_2}$:$\mathrm{Yb^{3+}}$ at ~1000 nm wavelength is typically <0.04 dB/cm [15], both α_p and α_s are considered to be negligible (i.e., $\alpha_p = \alpha_s = 0$), as compared with the absorption and emission terms in Eqs. (11) and (12).

To account for thermal effects, the power per unit volume deposited as heat in the device is determined by [45,46]

$$Q_{\mathrm{th}}(x, y, z) = \eta_h \alpha_{\mathrm{abs},p} I_p(0) \exp(-\alpha_{\mathrm{abs},p} z), \tag{13}$$

where η_h is the fractional heat load, and $\alpha_{\mathrm{abs},p}$ is the pump-absorption coefficient with a magnitude given by the expression within the square bracket in Eq. (11). $I_p(0)$ represents the incident pump intensity at $z = 0$ with a Gaussian profile as described by Eq. (3).

The fractional heat load η_h represents the fraction of absorbed pump power per unit volume which is converted into heat. It consists of the fractional heat loads originating in the quantum defect, η_{QD}, the ET process, η_{ET}, and the rapid quenching process, η_q:

$$\eta_h = f_a(\eta_{\mathrm{QD}} + \eta_{\mathrm{ET}}) + f_q \eta_q. \tag{14}$$

The quantum defect is defined by the fractional amount of absorbed photon energy which is converted to heat due to the difference of energy between the absorbed and emitted photons

$$\eta_{\mathrm{QD}} = 1 - \lambda_p/\lambda_m, \tag{15}$$

where λ_m is the mean emission wavelength estimated using

$$\lambda_m(T) = \int \lambda \sigma_{\mathrm{em}}(\lambda, T)\mathrm{d}\lambda \Big/ \int \sigma_{\mathrm{em}}(\lambda, T)\mathrm{d}\lambda. \tag{16}$$

Here, λ_m is chosen, because, in contrast with a laser, an amplifier operating in the small-signal-gain regime does not possess a single dominating emission wavelength. The chosen values are $\eta_{\mathrm{QD}} = \eta_{\mathrm{ET}} = 6.4\%$ and $\eta_q = 100\%$ (for further explanations, see Appendix A).

The temperature profile of the sample is governed by the heat-conduction equation and the boundary conditions between sample and external environment where the heat exchange occurs [47]:

$$-k_{\mathrm{th}} \nabla^2 T(x, y, z) = Q_{\mathrm{th}}(x, y, z), \tag{17}$$

$$\frac{\partial T}{\partial n} = h_T(T_{\mathrm{ext}} - T), \tag{18}$$

where k_{th} is the thermal conductivity, n is the normal to the boundary surface, h_T is the heat transfer coefficient, and T_{ext} is the external temperature of the thermal contact.

The three-dimensional optical-beam and thermal profiles were solved using a finite element method with *xyz* discretization (Comsol Multiphysics 5.3). The sets of solutions were obtained by solving Eqs. (1)–(3) and (8)–(18) self-consistently using material parameters given in Appendix A. Only a quarter of the sample was modeled to leverage the symmetry property of the sample and the propagating beams.

4. RESULTS AND DISCUSSION

A. Luminescence Decay

Luminescence-decay curves measured with different launched diode-laser power P_p are shown in Fig. 2. At a low P_p of 1.44 mW, the decay curve is close to an exponential decay. However, with increasing P_p, the detected decay curves exhibit an increasingly nonexponential decay, and an initial fast decay upon cutoff of the pump power is observed. The nonexponential decay behavior indicates that an ET process is present, which leads to additional depletion of the excited state. By simultaneously fitting the eight decay curves shown in Fig. 2 using Eq. (7), a W_{ET} value of 1.3×10^{-18} $\mathrm{cm^3/s}$ is extracted.

The presence of an energy-transfer process in an $\mathrm{Yb^{3+}}$-activated material is intriguing, as the $\mathrm{Yb^{3+}}$ ion has only two manifolds within the $4f$ subshell. Power-dependent nonexponential decay behavior similar to that observed in the present work was reported in YbAG crystals [27] and was attributed to cooperative energy transfer from two $\mathrm{Yb^{3+}}$ ions to an $\mathrm{Yb^{2+}}$ ion. However, the presence of $\mathrm{Yb^{2+}}$ has not yet been reported in $\mathrm{KRE(WO_4)_2}$:$\mathrm{Yb^{3+}}$, although it is known to exist in certain as-grown crystals such as YAG:$\mathrm{Yb^{3+}}$ [48] and LuAG:$\mathrm{Yb^{3+}}$ [49]. Given that the experimental data can be described by Bernoulli's Eq. (7), the observed energy-transfer behavior is possibly caused by cooperative upconversion

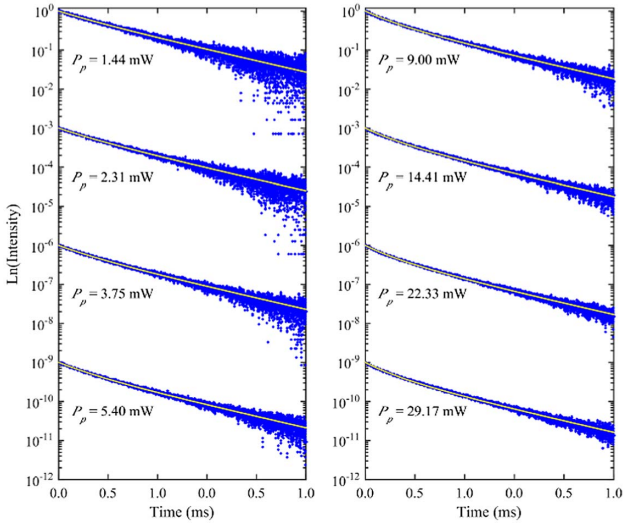

Fig. 2. Luminescence-decay curves (blue) measured with different launched diode-laser power P_p. The yellow lines represent fitted curves using Eq. (7).

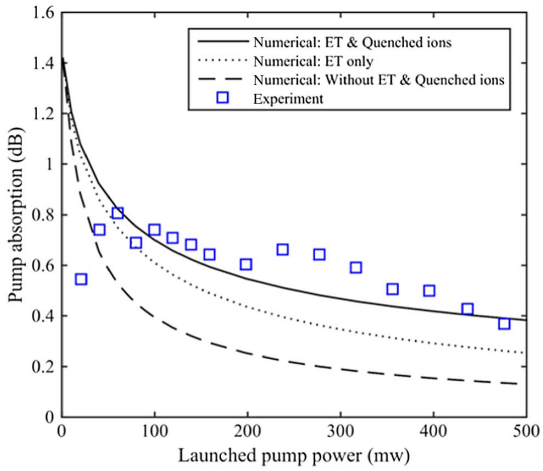

Fig. 3. Comparison of experimental pump-absorption data (squares) and pump-absorption results calculated with various settings (lines). The dashed line represents the modeled result without considering the ET process and quenched ions (i.e., $W_{\mathrm{ET}} = 0$ and $f_q = 0$). The dotted line shows the modeled result, which accounts for the ET process but not the quenched ions (i.e., $W_{\mathrm{ET}} = 1.3 \times 10^{-18}$ cm^3 s^{-1} and $f_q = 0$). The solid line is calculated with the consideration of both the ET process and quenched ions ($W_{\mathrm{ET}} = 1.3 \times 10^{-18}$ cm^3 s^{-1} and $f_q = 0.15$).

involving two excited Yb^{3+} ions in close proximity, forming a single quantum system and jointly emitting one green photon [50]. However, we have detected only weak green upconversion luminescence in the relevant spectral region besides small amounts of visible upconversion luminescence that can be attributed to Er^{3+} and Tm^{3+} impurities. At present, the exact physical mechanism responsible for the observed behavior remains unclear and may well be of a different nature. Answering this question would require a separate in-depth spectroscopic study, which is beyond the scope of the present work.

B. Pump Absorption

It is apparent from Eq. (13) that the heat generation in the sample is highly dependent on absorbed pump power. As such, the pump-absorption characteristic of the sample at 932 nm wavelength is investigated by comparing experimental and numerical results. The measured data points of pump absorption versus launched pump power are plotted in Fig. 3 as squares. The pump absorption is defined as

$$A_p = -10 \log_{10}[P_p(t_{\mathrm{layer}})/P_p(0)], \tag{19}$$

where $P_p(0)$ is the launched Ti:Sapphire pump power at the front surface, and $P_p(t_{\mathrm{layer}})$ is the residual pump power at the rear surface of the epitaxial layer after correcting for the transmittance of microscope objective and Fresnel reflection of the sample. The pump absorption calculated with the finite-element method using various sets of parameters is shown as lines in Fig. 3. These results consider the pump-induced heating, the changes of effective transition cross-sections due to temperature-dependent Boltzmann populations and transition linewidths, and thermal conductivities due to the heat generated within the layer.

The numerical result calculated using the typical model for Yb^{3+}-doped devices, i.e., without both ET process and quenched ions (dashed line in Fig. 3), show more intense saturation of pump absorption than the experimental results. The numerical result suggests that bleaching of the ground-state population should occur at high pump power, which in turn results in low fractional pump absorption at higher pump power. The ET process, as identified in the previous subsection, serves as an additional decay channel that depopulates the excited state. Therefore, the pump absorption calculated under consideration of the ET process (dotted line) is increased because a significant amount of ions is available in the ground state even when the pump intensity is high. Nevertheless, there is still a discrepancy between the experimental and numerical pump-absorption results, even though the ET process has been taken into account. The additional nonsaturable pump absorption is addressed by considering that ~15% of the Yb^{3+} ions are rapidly quenched, in addition to the ET process. In Al_2O_3:Yb^{3+}, a similar nonsaturable absorption was observed and attributed to 11% of Yb^{3+} ions being quenched at a dopant concentration of 6.6×10^{20} cm^{-3} [34]. The pump-absorption result calculated under consideration of these two factors is shown as a solid line in Fig. 3 and is in reasonable agreement with the experimental results. The fluctuations of the experimental data as compared with the calculated curve are likely due to the relatively large measurement uncertainty, which is estimated as ±0.17 dB when considering 2% of measurement uncertainty from the power meter. The stronger fluctuations at low pump power are due to inaccuracies of the thermal power-meter head at these low power levels.

C. Near-Infrared Luminescence Spectra

Figure 4(a) shows the near-infrared luminescence spectra at various launched pump-power values P_p. Three emission peaks are observed at ~981, ~1000, and ~1023 nm wavelengths that correspond to the $E_{10} \rightarrow E_{00}, E_{10} \rightarrow E_{01}$, and $E_{10} \rightarrow E_{02}$

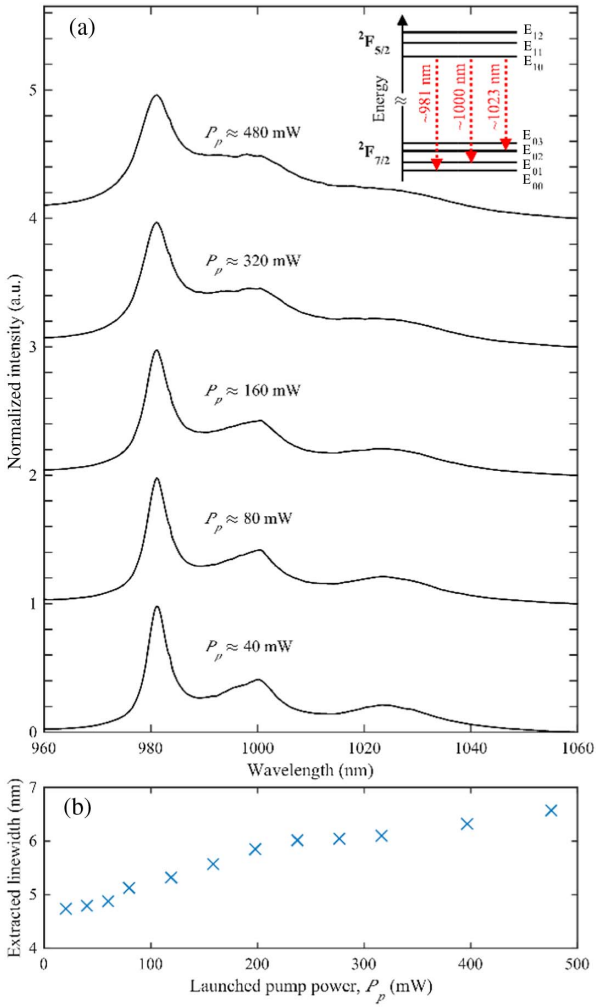

Fig. 4. (a) Normalized luminescence spectra recorded with different Ti:Sapphire launched pump power P_p. The inset illustrates the relevant transitions contributing to a large part of the observed emission at the corresponding wavelength. (b) Evolution of the linewidth (FWHM) of the decomposed peak at ~981 nm with increasing P_p.

transitions, respectively; see the inset of Fig. 4(a). With increasing pump power, a smoothening emission spectrum is observed, and the emission peaks at 1000 and 1023 nm wavelengths become less distinguishable. In addition, the ratio of the magnitude of the 981 nm emission peak to that of the 1000 nm emission peak decreases with increasing P_p. This is in contrast to the typical case of amplified spontaneous emission, in which the emission peak at 981 nm would narrow and increase with higher pump power.

Further analysis was performed on the spectra via multiple-peak fitting by assuming three Lorentzian peaks using a data-analysis program (Origin 9.1). The extracted full-width-at-half-maximum (FWHM) values for the main emission peak at 981 nm wavelength for different P_p values are plotted in Fig. 4(b). A significant increase in FWHM is evident over the entire P_p range investigated. The linewidth broadening is in line with the temperature-dependent behavior of the emission cross-section spectra [6], signifying that a thermal effect is present in the gain medium even under low P_p.

D. Small-Signal Gain

During the pump–probe experiment, the lock-in signal intensity is recorded when the pump is launched (I_{on}) and when the pump is blocked (I_{off}). The signal enhancement is defined by the expression

$$\gamma = 10\log_{10}(I_{on}/I_{off}). \tag{20}$$

The net gain per unit length, g, of the sample is determined by

$$g = (\gamma/t_{layer}) - \alpha_{total}, \tag{21}$$

where α_{total} is the total signal loss per unit length due to propagation loss α_s and absorption by the unpumped Yb^{3+} ions:

$$\alpha_{total} = \alpha_s + 10 \cdot \log_{10} e \cdot \sigma_{abs}(\lambda_s, T) \cdot N_{Yb}. \tag{22}$$

As mentioned in Section 3, the propagation loss α_s is typically <0.04 dB/cm [15]; hence, it is negligible as compared with the absorption loss due to Yb^{3+} ions in the epitaxial layer, $10\log_{10} e\sigma_{abs}(\lambda_s, T)N_{Yb}$. During the experiment, I_{on} was recorded first in the presence of the pump beam, and I_{off} was recorded right after the pump beam was blocked. Therefore, it is assumed that the pump-induced heating persists, as the dissipation of heat would take place at a comparatively longer time scale. Consequently, the absorption loss due to Yb^{3+} ions in the ground state is deduced using the calculated averaged temperature T_p within the pumped volume, $V_p \approx \pi w_p^2 t_{layer}$, and the net gain per unit length is calculated accordingly.

The experimental and modeled signal-enhancement results are shown in Fig. 5(a). The maximum signal enhancement measured at ~475 mW launched pump power is 8.13 dB. The modeled signal enhancement under consideration of the ET process, 15% quenched ions, and thermal effects is in reasonable agreement with the experimental results. The numerical calculation shows that T_p can rise from 27°C with pump off to 62.8°C at $P_l = 475$ mW. Considering in Eq. (22) the reduced absorption cross-section of 1.058×10^{-19} cm^2 calculated at $T_p = 62.8$°C, a total signal absorption of 5.59 dB is deduced. Consequently, a peak net-gain value of 2.54 dB, or 793.75 dB/cm, is obtained based on the signal-enhancement data.

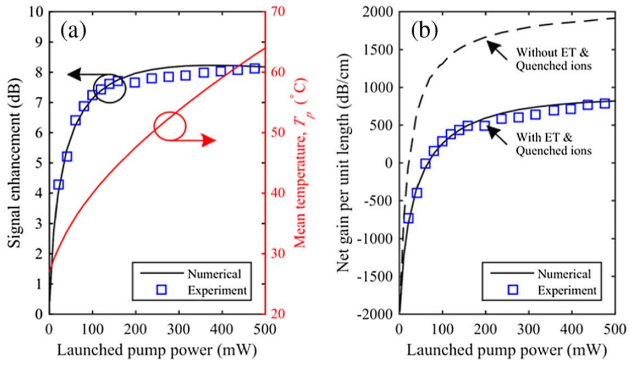

Fig. 5. (a) Experimental and modeled signal enhancement. The calculated mean temperature within the pump volume is shown on the right y axis. (b) Corresponding results of net gain per unit length. The net gain per unit length calculated without considering the ET process and quenched ions is shown in (b) as a dashed line.

Comparison of the modeled gain in Fig. 5(b) reveals a marked difference in gain performance when considering the usual gain model for Yb^{3+}-doped media and our proposed model. The usual gain model does not include an ET process and quenched ions; hence, the heat generation is mainly owing to the quantum defect which is inherently low in Yb^{3+}-doped devices. The peak gain deduced from such a model (dashed line) is ~1900 dB/cm at $P_l = 500$ mW. The gain model proposed in this work includes an ET process, which causes depletion of the excited-state population. Moreover, further consideration of 15% of quenched ions implies that only the remaining 85% of active ions are participating in the signal-amplification process. In addition, the substantial increase of heating causes a reduction of the transition cross-sections with increasing pump power. As a result, the gain calculated with the proposed model (solid line) is effectively clamped to ~820 dB/cm at 500 mW of launched pump power. The experiment was conducted without thermal management. Despite this, the net gain per unit length obtained is more than an order of magnitude higher than in other Yb^{3+}- or Nd^{3+}-doped waveguide amplifiers [23–26] and even comparable with the modal gain of a III-V semiconductor amplifier. The promising gain results also indicate that a $KGd_{0.43}Yb_{0.57}(WO_4)_2$ epitaxial layer is well suited for the realization of a millimeter-scale waveguide amplifier that can operate without a Peltier element. Further improvement of the gain performance is anticipated with the use of passive or active thermal management.

5. CONCLUSIONS

The optical properties of a $KGd_{0.43}Yb_{0.57}(WO_4)_2$ epitaxial film with an Yb^{3+} concentration as high as $\sim 3.8 \times 10^{21}$ cm^{-3} were examined via experimental and numerical methods. A parasitic energy-transfer process and quenched ions were observed under intense excitation conditions, and the relevant parameters were quantified. Besides, the broadening of emission spectra with increasing pump power signifies the presence of thermal effects even at low pump power. A gain model which takes into account the energy-transfer process, quenched ions, and thermal effects is presented in this work. Our model provides insights into the impact of these nondesired effects on the attainable gain in an epitaxial film with high Yb^{3+} concentration. The numerical signal enhancement is in agreement with the measurement result, and a peak signal enhancement of 8.13 dB is obtained at 981 nm wavelength. Our calculation shows that the temperature of the pumped volume may elevate to >60°C; hence, the change of effective transition cross-sections with pump power is non-negligible. Nevertheless, a peak net gain of ~800 dB/cm is attainable without thermal management; hence, the material is promising for realizing waveguide amplifiers that can operate without active cooling.

APPENDIX A: MATERIAL PARAMETERS

The sample used for the investigation of material gain consists of a 32 μm thick $KGd_{0.43}Yb_{0.57}(WO_4)_2$ layer grown onto an undoped $KY(WO_4)_2$ substrate. Relevant parameters of the epitaxial layer and the substrate, which are used in the numerical calculations, are summarized in Table 1.

Table 1. Parameters Used for Numerical Modeling

Parameter	Value
Layer composition	$KGd_{0.43}Yb_{0.57}(WO_4)_2$
Thickness of polished layer, t_{layer}	32 μm
Yb^{3+} concentration, N_{Yb}	3.8×10^{21} cm^{-3}
Substrate	$KY(WO_4)_2$
Substrate thickness, $t_{substrate}$	~1 mm
Substrate width, $w_{substrate}$	~10 mm
Substrate depth, $d_{substrate}$	~10 mm
Gaussian beam waist for pump, w_p	5 μm
Gaussian beam waist for signal, w_s	4 μm
Pump wavelength, λ_p	932 nm
Signal wavelength, λ_s	981 nm
Mean emission wavelength, λ_m	996 nm
Propagation losses, α_p & α_s	0 dB/cm
Luminescence lifetime, τ_a	228 μs [39]
Energy-transfer parameter, W_{ET}	1.3×10^{-18} cm^3 s^{-1}
Fraction of quenched ions, f_q	0 or 0.15
Heat-transfer coefficient, h_T	10 Wm^{-2} K^{-1}
External temperature, T_{ext}	300 K

For ease of numerical calculation, a generic empirical formula adapted from [51] is used here for all temperature-dependent parameters:

$$X(T) = X(T_0)(1 + c_1 T + c_2 T^2 + c_3 T^3), \quad \textbf{(A1)}$$

where X is the parameter of interest, T_0 is an arbitrary reference temperature, and c_1, c_2, and c_3 are fitted parameters.

The temperature-dependent effective transition cross-sections [6] and luminescence lifetime value of 228 μs [39] measured from the same sample are used for the numerical calculation. The transition cross-sections for the polarization $E||N_m$ as a function of temperature are plotted in Fig. 6(a) as symbols. The corresponding fitted curves using Eq. (A1) are displayed as lines in the figure. The relevant fitted parameters can be found in Table 2. The luminescence lifetime, on the other hand, has no significant dependence on the sample temperature [6].

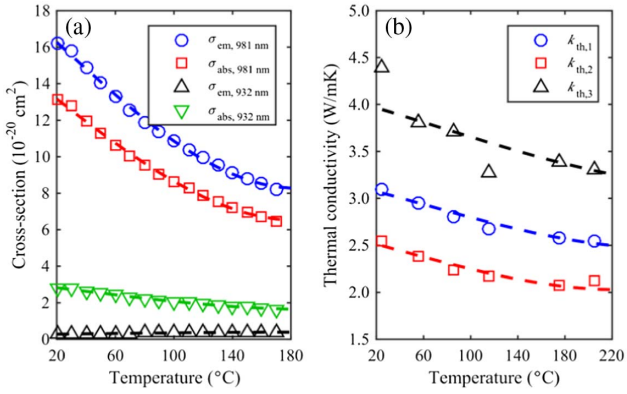

Fig. 6. Temperature-dependent data of (a) effective transition cross-sections for the polarization $E||N_m$ extracted from [6] and (b) thermal conductivities $k_{th,1}$, $k_{th,2}$, and $k_{th,3}$ for the respective thermal axis of X'_1, X'_2, and X'_3 (data from [52]). The lines are plotted from Eq. (A1) using the least-squares fitted parameters listed in Tables 2 and 3.

Table 2. Parameters for Effective Transition Cross-Sections

Parameter[a] (unit)	T_0 (K)	σ (T_0) (10^{-20} cm^2)	c_1 (10^{-3} K^{-1})	c_2 (10^{-5} K^{-2})	c_3 (10^{-8} K^{-3})
$\sigma_{abs,932\,nm}$	293.15	2.81	7.063	−3.574	4.004
$\sigma_{em,932\,nm}$	293.15	0.267	−7.527	3.925	−4.512
$\sigma_{abs,981\,nm}$	293.15	13.1	9.598	−4.933	5.672
$\sigma_{em,981\,nm}$	293.15	16.2	9.301	−4.775	5.482

[a]Applicable for temperature range within 293.15–443.15 K.

Table 3. Parameters for Thermal Conductivities

Parameter[a] (unit)	T_0 (K)	$k(T_0)$ (Wm^{-1} K^{-1})	c_1(10^{-3} K^{-1})	c_2(10^{-5} K^{-2})	c_3(10^{-8} K^{-3})
$k_{th,1}$	298.15	3.09	1.851	−0.9055	0.9155
$k_{th,2}$	298.15	2.55	2.298	−1.170	1.257
$k_{th,3}$	298.15	4.00	1.402	−0.6786	0.6439

[a]Applicable for temperature range within 293.15–493.15 K.

The temperature-dependent thermal conductivities reported for Yb^{3+}-doped $KLu(WO_4)_2$ [52] are used here, as there is a lack of comprehensive temperature-dependent data for other double tungstates. Figure 6(b) shows the thermal conductivities $k_{th,1}$, $k_{th,2}$, and $k_{th,3}$ for the respective thermal axis of X_1, X_2, and X_3. The thermal axis X_2 coincides with the N_p optical axis, and both are parallel to the direction of beam propagation in the gain experiment. Relevant fitted values are provided in Table 3.

The external temperature T_{ext} is assumed to be 300 K, as no active cooling was applied to the sample. The value of heat transfer coefficient h_T is highly dependent on the thermal interfaces of the sample during the experiment and is typically regarded as a freely adjustable parameter for thermal calculations. A typical h_T value accounting for surface radiation and convection between the air/sample interfaces is ∼10 Wm^{-2} K^{-1} for each of the two cases [53,54], whereas the h_T value for a sample in bare contact with a water-cooled copper holder can be as high as 2500 Wm^{-2} K^{-1} [55]. Because only a small part of the $KGd_{0.43}Yb_{0.57}(WO_4)_2$ sample was clamped by two small copper plates during the measurements, and no special effort was applied to improve the thermal contact between the sample and the holder, a rather conservative h_T value of 10 Wm^{-2} K^{-1} is employed for all sample surfaces in the numerical calculation.

The mean emission wavelength λ_m calculated from the temperature-dependent σ_{em} spectra measured in previous work [6] using Eq. (16) is 996.14 ± 1.3 nm throughout the temperature range of 20–170°C, which is in good agreement with the average luminescence wavelength of 997 nm, as reported in [56]. There could be a small dependence of λ_m on temperature because the value of σ_{em} beyond 1050 nm wavelength is associated with high uncertainty and not considered in the calculation. Consequently, the fractional heat load due to the quantum defect η_{QD} is calculated as 6.4%. The total energy associated with the fast decay of quenched ions is expected to result entirely in the generation of phonons; hence, η_q is 100%. It is assumed that the heat load generated by the parasitic energy-transfer process is equal to η_{QD}, i.e., $\eta_{ET} = \eta_{QD}$, due the uncertain nature of the process. In any case, an assumption that results in a higher η_{ET} can be balanced by an accordingly higher h_T because there are high uncertainties associated with both parameters. With these considerations, the fractional heat load used for the numerical calculation is

$$\eta_h = f_a(6.4\%) + f_q(100\%). \tag{A2}$$

The Gaussian beam waists of the focused pump beam w_p and signal beam w_s listed in Table 1 are based on measured beam profiles. To ensure high pump intensity and optimum pump-signal overlap, the beam sizes in the experiment were chosen to be as small as possible, while ensuring that their confocal lengths (i.e., twice the Rayleigh length) are longer than the layer thickness.

Funding. Stichting voor de Technische Wetenschappen (STW) (11689).

REFERENCES

1. N. V. Kuleshov, A. A. Lagatsky, A. V. Podlipensky, V. P. Mikhailov, and G. Huber, "Pulsed laser operation of Yb-doped $KY(WO_4)_2$ and $KGd(WO_4)_2$," Opt. Lett. **22**, 1317–1319 (1997).
2. J. E. Hellström, B. Jacobsson, V. Pasiskevicius, and F. Laurell, "Quasi-two-level Yb:KYW laser with a volume Bragg grating," Opt. Express **15**, 13930–13935 (2007).
3. M. T. Chang, H. C. Liang, K. W. Su, and Y. F. Chen, "Dual-comb self-mode-locked monolithic Yb:KGW laser with orthogonal polarizations," Opt. Express **23**, 10111–10116 (2015).
4. J. Liu, V. Petrov, X. Mateos, H. Zhang, and J. Wang, "Efficient high-power laser operation of Yb:$KLu(WO_4)_2$ crystals cut along the principal optical axes," Opt. Lett. **32**, 2016–2018 (2007).
5. K. Petermann, D. Fagundes-Peters, J. Johannsen, M. Mond, V. Peters, J. J. Romero, S. Kutovoi, J. Speiser, and A. Giesen, "Highly Yb-doped oxides for thin-disc lasers," J. Cryst. Growth **275**, 135–140 (2005).
6. Y. S. Yong, S. Aravazhi, S. A. Vázquez-Córdova, J. J. Carjaval, F. Díaz, J. L. Herek, S. M. García-Blanco, and M. Pollnau, "Temperature-dependent absorption and emission of potassium double tungstates with high ytterbium content," Opt. Express **24**, 26825–26837 (2016).
7. J. Koerner, C. Vorholt, H. Liebetrau, M. Kahle, D. Kloepfel, R. Seifert, J. Hein, and M. C. Kaluza, "Measurement of temperature-dependent absorption and emission spectra of Yb:YAG, Yb:LuAG, and Yb:CaF_2 between 20°C and 200°C and predictions on their influence on laser performance," J. Opt. Soc. Am. B **29**, 2493–2502 (2012).

8. F. Gardillou, Y. E. Romanyuk, C. N. Borca, R.-P. Salathé, and M. Pollnau, "Lu, Gd codoped $KY(WO_4)_2$:Yb epitaxial layers: towards integrated optics based on $KY(WO_4)_2$," Opt. Lett. **32**, 488–490 (2007).
9. M. Pollnau, Y. E. Romanyuk, F. Gardillou, C. N. Borca, U. Griebner, S. Rivier, and V. Petrov, "Double tungstate lasers: from bulk toward on-chip integrated waveguide devices," IEEE J. Sel. Top. Quantum Electron. **13**, 661–671 (2007).
10. S. Aravazhi, D. Geskus, K. van Dalfsen, S. A. Vázquez-Córdova, C. Grivas, U. Griebner, S. M. García-Blanco, and M. Pollnau, "Engineering lattice matching, doping level, and optical properties of $KY(WO_4)_2$:Gd, Lu, Yb layers for a cladding-side-pumped channel waveguide laser," Appl. Phys. B **111**, 433–446 (2013).
11. D. Geskus, S. Aravazhi, E. Bernhardi, C. Grivas, S. Harkema, K. Hametner, D. Günther, K. Wörhoff, and M. Pollnau, "Low-threshold, highly efficient Gd^{3+}, Lu^{3+} co-doped $KY(WO_4)_2$:Yb^{3+} planar waveguide lasers," Laser Phys. Lett. **6**, 800–805 (2009).
12. J. W. Kim, S. Y. Choi, D. I. Yeom, S. Aravazhi, M. Pollnau, U. Griebner, V. Petrov, and F. Rotermund, "Yb:KYW planar waveguide laser Q-switched by evanescent-field interaction with carbon nanotubes," Opt. Lett. **38**, 5090–5093 (2013).
13. J. W. Kim, S. Y. Choi, S. Aravazhi, M. Pollnau, U. Griebner, V. Petrov, S. Bae, K. J. Ahn, D. I. Yeom, and F. Rotermund, "Graphene Q-switched Yb:KYW planar waveguide laser," AIP Adv. **5**, 017110 (2015).
14. F. M. Bain, A. A. Lagatsky, S. V. Kurilchick, V. E. Kisel, S. A. Guretsky, A. M. Luginets, N. A. Kalanda, I. M. Kolesova, N. V. Kuleshov, W. Sibbett, and C. T. Brown, "Continuous-wave and Q-switched operation of a compact, diode-pumped Yb^{3+}:$KY(WO_4)_2$ planar waveguide laser," Opt. Express **17**, 1666–1670 (2009).
15. D. Geskus, S. Aravazhi, C. Grivas, K. Wörhoff, and M. Pollnau, "Microstructured $KY(WO_4)_2$:Gd^{3+}, Lu^{3+}, Yb^{3+} channel waveguide laser," Opt. Express **18**, 8853–8858 (2010).
16. D. Geskus, E. H. Bernhardi, K. van Dalfsen, S. Aravazhi, and M. Pollnau, "Highly efficient Yb^{3+}-doped channel waveguide laser at 981 nm," Opt. Express **21**, 13773–13778 (2013).
17. D. Geskus, S. Aravazhi, K. Wörhoff, and M. Pollnau, "High-power, broadly tunable, and low-quantum-defect $KGd_{1-x}Lu_x(WO_4)_2$:Yb^{3+} channel waveguide lasers," Opt. Express **18**, 26107–26112 (2010).
18. D. Geskus, S. Aravazhi, S. M. García-Blanco, and M. Pollnau, "Giant optical gain in a rare-earth-ion-doped microstructure," Adv. Mater. **24**, OP19–OP22 (2012).
19. F. E. Doany, C. L. Schow, C. W. Baks, D. M. Kuchta, P. Pepeljugoski, L. Schares, R. Budd, F. Libsch, R. Dangel, F. Horst, B. J. Offrein, and J. A. Kash, "160 Gb/s bidirectional polymer-waveguide board-level optical interconnects using CMOS-based transceivers," IEEE Trans. Adv. Packag. **32**, 345–359 (2009).
20. J. B. Héroux, T. Kise, M. Funabashi, T. Aoki, C. L. Schow, A. V. Rylyakov, and S. Nakagawa, "Energy-efficient 1060-nm optical link operating up to 28 Gb/s," J. Lightwave Technol. **33**, 733–740 (2015).
21. H. Nasu, Y. Ishikawa, Y. Nekado, M. Yoshihara, A. Izawa, T. Uemura, and K. Takahashi, "1060-nm VCSEL-based parallel-optical modules for short link applications," in *Conference on Optical Fiber Communication (OFC), Collocated National Fiber Optic Engineers Conference (OFC/NFOEC)* (IEEE, 2010), paper OThC1.
22. J. Yang, T. Lamprecht, K. Wörhoff, A. Driessen, F. Horst, B. J. Offrein, F. Ay, and M. Pollnau, "Integrated optical backplane amplifier," IEEE J. Sel. Top. Quantum Electron. **17**, 609–616 (2011).
23. A. Aghajani, G. S. Murugan, N. P. Sessions, S. J. Pearce, V. Apostolopoulos, and J. S. Wilkinson, "Spectroscopy of ytterbium-doped tantalum pentoxide rib waveguides on silicon," Opt. Mater. Express **4**, 1505–1514 (2014).
24. J. Yang, K. van Dalfsen, K. Wörhoff, F. Ay, and M. Pollnau, "High-gain Al_2O_3:Nd^{3+} channel waveguide amplifiers at 880 nm, 1060 nm, and 1330 nm," Appl. Phys. B **101**, 119–127 (2010).
25. J. Yang, M. B. J. Diemeer, G. Sengo, M. Pollnau, and A. Driessen, "Nd-doped polymer waveguide amplifiers," IEEE J. Quantum Electron. **46**, 1043–1050 (2010).
26. Y. Tan, Q. Luan, F. Liu, S. Akhmadaliev, S. Zhou, and F. Chen, "Swift carbon ion irradiated Nd:YAG ceramic optical waveguide amplifier," Opt. Express **21**, 13992–13997 (2013).
27. D. Fagundes-Peters, N. Martynyuk, K. Lünstedt, V. Peters, K. Petermann, G. Huber, S. Basun, V. Laguta, and A. Hofstaetter, "High quantum efficiency YbAG-crystals," J. Lumin. **125**, 238–247 (2007).
28. L. Agazzi, K. Wörhoff, and M. Pollnau, "Energy-transfer-upconversion models, their applicability and breakdown in the presence of spectroscopically distinct ion classes: a case study in amorphous Al_2O_3:Er^{3+}," J. Phys. Chem. C **117**, 6759–6776 (2013).
29. S. Banerjee, C. C. Baker, A. J. Steckl, and D. Klotzkin, "Optical properties of Er in Er-doped $Zn_2Si_{0.5}Ge_{0.5}O_4$ waveguide amplifiers," J. Lightwave Technol. **23**, 1342–1349 (2005).
30. E. Delevaque, T. Georges, M. Monerie, P. Lamouler, and J. F. Bayon, "Modeling of pair-induced quenching in erbium-doped silicate fibers," IEEE Photon. Technol. Lett. **5**, 73–75 (1993).
31. E. Maurice, G. Monnom, B. Dussardier, and D. B. Ostrowsky, "Clustering-induced nonsaturable absorption phenomenon in heavily erbium-doped silica fibers," Opt. Lett. **20**, 2487–2489 (1995).
32. R. Paschotta, J. Nilsson, P. R. Barber, J. E. Caplen, A. C. Tropper, and D. C. Hanna, "Lifetime quenching in Yb-doped fibres," Opt. Commun. **136**, 375–378 (1997).
33. Z. Burshtein, Y. Kalisky, S. Z. Levy, P. Le Boulanger, and S. Rotman, "Impurity local phonon nonradiative quenching of Yb^{3+} fluorescence in ytterbium-doped silicate glasses," IEEE J. Quantum Electron. **36**, 1000–1007 (2000).
34. L. Agazzi, E. H. Bernhardi, K. Wörhoff, and M. Pollnau, "Impact of luminescence quenching on relaxation-oscillation frequency in solid-state lasers," Appl. Phys. Lett. **100**, 011109 (2012).
35. M. Larionov, K. Schuhmann, J. Speiser, C. Stolzenburg, and A. Giesen, "Nonlinear decay of the excited state in Yb:YAG," in *Advanced Solid-State Photonics*, Technical Digest (Optical Society of America, 2005), paper TuB49.
36. V. Petrov, M. C. Pujol, X. Mateos, Ò. Silvestre, S. Rivier, M. Aguiló, R. M. Solé, J. Liu, U. Griebner, and F. Díaz, "Growth and properties of $KLu(WO_4)_2$, and novel ytterbium and thulium lasers based on this monoclinic crystalline host," Laser Photon. Rev. **1**, 179–212 (2007).
37. P. Klopp, U. Griebner, V. Petrov, X. Mateos, M. A. Bursukova, M. C. Pujol, R. Sole, J. Gavalda, M. Aguilo, F. Güell, J. Massons, T. Kirilov, and F. Diaz, "Laser operation of the new stoichiometric crystal $KYb(WO_4)_2$," Appl. Phys. B **74**, 185–189 (2002).
38. C. Brandt, S. T. Fredrich-Thornton, K. Petermann, and G. Huber, "Photoconductivity in Yb-doped oxides at high excitation densities," Appl. Phys. B **102**, 765–768 (2011).
39. Y. S. Yong, S. Aravazhi, S. A. Vázquez-Córdova, J. J. Carvajal, F. Díaz, J. L. Herek, S. M. García-Blanco, and M. Pollnau, "Direct confocal lifetime measurements on rare-earth-doped media exhibiting radiation trapping," Opt. Mater. Express **7**, 527–532 (2017).
40. D. S. Sumida and T. Y. Fan, "Effect of radiation trapping on fluorescence lifetime and emission cross section measurements in solid-state laser media," Opt. Lett. **19**, 1343–1345 (1994).
41. R. Paschotta, J. Nilsson, A. C. Tropper, and D. C. Hanna, "Ytterbium-doped fiber amplifiers," IEEE J. Quantum Electron. **33**, 1049–1056 (1997).
42. B. Jacobsson, "Experimental and theoretical investigation of a volume-Bragg-grating-locked Yb:KYW laser at selected wavelengths," Opt. Express **16**, 6443–6454 (2008).
43. W. J. C. Grant, "Role of rate equations in the theory of luminescent energy transfer," Phys. Rev. B **4**, 648–663 (1971).
44. P. S. Golding, S. D. Jackson, T. A. King, and M. Pollnau, "Energy transfer processes in Er^{3+}-doped and Er^{3+}, Pr^{3+}-codoped ZBLAN glasses," Phys. Rev. B **62**, 856–864 (2000).
45. M. E. Innocenzi, H. T. Yura, C. L. Fincher, and R. A. Fields, "Thermal modeling of continuous-wave end-pumped solid-state lasers," Appl. Phys. Lett. **56**, 1831–1833 (1990).
46. P. A. Loiko, K. V. Yumashev, N. V. Kuleshov, and A. A. Pavlyuk, "Comparative thermal analysis of Nd- and Yb-doped YAG and KGdW laser crystals under diode- and flashlamp-pumping," Opt. Laser Technol. **44**, 2232–2237 (2012).
47. S. Chénais, F. Druon, S. Forget, F. Balembois, and P. Georges, "On thermal effects in solid-state lasers: the case of ytterbium-doped materials," Prog. Quantum Electron. **30**, 89–153 (2006).

48. X. Xu, Z. Zhao, P. Song, G. Zhou, J. Xu, and P. Deng, "Structural, thermal, and luminescent properties of Yb-doped $Y_3Al_5O_{12}$ crystals," J. Opt. Soc. Am. B **21**, 543–547 (2004).
49. D. Luo, J. Zhang, C. Xu, H. Yang, H. Lin, H. Zhu, and D. Tang, "Yb:LuAG laser ceramics: a promising high power laser gain medium," Opt. Mater. Express **2**, 1425–1431 (2012).
50. E. Nakazawa and S. Shionoya, "Cooperative luminescence in $YbPO_4$," Phys. Rev. Lett. **25**, 1710–1712 (1970).
51. Y. Sato and T. Taira, "Temperature dependencies of stimulated emission cross section for Nd-doped solid-state laser materials," Opt. Mater. Express **2**, 1076–1087 (2012).
52. J. Zhang, K. Wang, J. Wang, H. Zhang, W. Yu, X. Wang, Z. Wang, Q. Lu, M. Ba, D. G. Ran, Z. C. Ling, and H. R. Xia, "Anisotropic thermal properties of monoclinic Yb:$KLu(WO_4)_2$ crystals," Appl. Phys. Lett. **87**, 061104 (2005).
53. A. K. Cousins, "Temperature and thermal stress scaling in finite-length end-pumped laser rods," IEEE J. Quantum Electron. **28**, 1057–1069 (1992).
54. S. Chénais, F. Balembois, F. Druon, G. Lucas-Leclin, and P. Georges, "Thermal lensing in diode-pumped ytterbium lasers-Part I: theoretical analysis and wavefront measurements," IEEE J. Quantum Electron. **40**, 1217–1234 (2004).
55. S. Chénais, S. Forget, F. Druon, F. Balembois, and P. Georges, "Direct and absolute temperature mapping and heat transfer measurements in diode-end-pumped Yb:YAG," Appl. Phys. B **79**, 221–224 (2004).
56. S. Biswal, S. P. O'Connor, and S. R. Bowman, "Nonradiative losses in Yb:$KGd(WO_4)_2$ and Yb:$Y_3Al_5O_{12}$," Appl. Phys. Lett. **89**, 091911 (2006).